CrossMark

Investigating the Nature of Late-time High-energy GRB Emission through Joint *Fermi*/*Swift* Observations

M. Ajello[1], L. Baldini[2], G. Barbiellini[3,4], D. Bastieri[5,6], R. Bellazzini[7], E. Bissaldi[8,9], R. D. Blandford[10], R. Bonino[11,12], E. Bottacini[10], J. Bregeon[13], P. Bruel[14], R. Buehler[15], R. A. Cameron[10], R. Caputo[16], P. A. Caraveo[17], G. Chiaro[17], S. Ciprini[18,19], J. Cohen-Tanugi[13], D. Costantin[6], F. D'Ammando[20,21], F. de Palma[9,22], N. Di Lalla[2], M. Di Mauro[10], L. Di Venere[8,9], A. Domínguez[23], C. Favuzzi[8,9], A. Franckowiak[15], Y. Fukazawa[24], S. Funk[25], P. Fusco[8,9], F. Gargano[9], D. Gasparrini[18,19], N. Giglietto[8,9], F. Giordano[8,9], M. Giroletti[20], D. Green[26,27], I. A. Grenier[28], S. Guiriec[27,29], C. Holt[30], D. Horan[14], G. Jóhannesson[31,32], D. Kocevski[27], M. Kuss[7], G. La Mura[6], S. Larsson[33,34], J. Li[35], F. Longo[3,4], F. Loparco[8,9], P. Lubrano[19], J. D. Magill[26], S. Maldera[11], A. Manfreda[2], M. N. Mazziotta[9], P. F. Michelson[10], T. Mizuno[36], M. E. Monzani[10], A. Morselli[37], M. Negro[11,12], E. Nuss[13], N. Omodei[10], M. Orienti[20], E. Orlando[10], V. S. Paliya[1], J. S. Perkins[27], M. Persic[3,38], M. Pesce-Rollins[7], F. Piron[13], G. Principe[25], J. L. Racusin[27], S. Rainò[8,9], R. Rando[5,6], M. Razzano[7,46], S. Razzaque[39], A. Reimer[10,40], O. Reimer[10,40], C. Sgrò[7], E. J. Siskind[41], G. Spandre[7], P. Spinelli[8,9], D. Tak[26,27], J. B. Thayer[10], D. F. Torres[35,42], G. Tosti[19,43], J. Valverde[14], M. Vogel[44], and K. Wood[45]

[1] Department of Physics and Astronomy, Clemson University, Kinard Lab of Physics, Clemson, SC 29634-0978, USA
[2] Università di Pisa and Istituto Nazionale di Fisica Nucleare, Sezione di Pisa I-56127 Pisa, Italy
[3] Istituto Nazionale di Fisica Nucleare, Sezione di Trieste, I-34127 Trieste, Italy
[4] Dipartimento di Fisica, Università di Trieste, I-34127 Trieste, Italy
[5] Istituto Nazionale di Fisica Nucleare, Sezione di Padova, I-35131 Padova, Italy
[6] Dipartimento di Fisica e Astronomia "G. Galilei," Università di Padova, I-35131 Padova, Italy
[7] Istituto Nazionale di Fisica Nucleare, Sezione di Pisa, I-56127 Pisa, Italy
[8] Dipartimento di Fisica "M. Merlin" dell'Università e del Politecnico di Bari, I-70126 Bari, Italy
[9] Istituto Nazionale di Fisica Nucleare, Sezione di Bari, I-70126 Bari, Italy
[10] W. W. Hansen Experimental Physics Laboratory, Kavli Institute for Particle Astrophysics and Cosmology, Department of Physics and SLAC National Accelerator Laboratory, Stanford University, Stanford, CA 94305, USA
[11] Istituto Nazionale di Fisica Nucleare, Sezione di Torino, I-10125 Torino, Italy
[12] Dipartimento di Fisica, Università degli Studi di Torino, I-10125 Torino, Italy
[13] Laboratoire Univers et Particules de Montpellier, Université Montpellier, CNRS/IN2P3, F-34095 Montpellier, France
[14] Laboratoire Leprince-Ringuet, École polytechnique, CNRS/IN2P3, F-91128 Palaiseau, France
[15] Deutsches Elektronen Synchrotron DESY, D-15738 Zeuthen, Germany
[16] Center for Research and Exploration in Space Science and Technology (CRESST) and NASA Goddard Space Flight Center, Greenbelt, MD 20771, USA
[17] INAF-Istituto di Astrofisica Spaziale e Fisica Cosmica Milano, via E. Bassini 15, I-20133 Milano, Italy
[18] Space Science Data Center—Agenzia Spaziale Italiana, Via del Politecnico, snc, I-00133, Roma, Italy
[19] Istituto Nazionale di Fisica Nucleare, Sezione di Perugia, I-06123 Perugia, Italy
[20] INAF Istituto di Radioastronomia, I-40129 Bologna, Italy
[21] Dipartimento di Astronomia, Università di Bologna, I-40127 Bologna, Italy
[22] Università Telematica Pegaso, Piazza Trieste e Trento, 48, I-80132 Napoli, Italy
[23] Grupo de Altas Energías, Universidad Complutense de Madrid, E-28040 Madrid, Spain
[24] Department of Physical Sciences, Hiroshima University, Higashi-Hiroshima, Hiroshima 739-8526, Japan
[25] Friedrich-Alexander-Universität Erlangen-Nürnberg, Erlangen Centre for Astroparticle Physics, Erwin-Rommel-Str. 1, D-91058 Erlangen, Germany
[26] Department of Astronomy, University of Maryland, College Park, MD 20742, USA
[27] NASA Goddard Space Flight Center, Greenbelt, MD 20771, USA; daniel.kocevski@nasa.gov, judith.racusin@nasa.gov
[28] Laboratoire AIM, CEA-IRFU/CNRS/Université Paris Diderot, Service d'Astrophysique, CEA Saclay, F-91191 Gif sur Yvette, France
[29] The George Washington University, Department of Physics, 725 21st St., NW, Washington, DC 20052, USA
[30] Department of Physics and Center for Space Sciences and Technology, University of Maryland Baltimore County, Baltimore, MD 21250, USA
[31] Science Institute, University of Iceland, IS-107 Reykjavik, Iceland
[32] Nordita, Roslagstullsbacken 23, SE-106 91 Stockholm, Sweden
[33] Department of Physics, KTH Royal Institute of Technology, AlbaNova, SE-106 91 Stockholm, Sweden
[34] The Oskar Klein Centre for Cosmoparticle Physics, AlbaNova, SE-106 91 Stockholm, Sweden
[35] Institute of Space Sciences (CSICIEEC), Campus UAB, Carrer de Magrans s/n, E-08193 Barcelona, Spain
[36] Hiroshima Astrophysical Science Center, Hiroshima University, Higashi-Hiroshima, Hiroshima 739-8526, Japan
[37] Istituto Nazionale di Fisica Nucleare, Sezione di Roma "Tor Vergata," I-00133 Roma, Italy
[38] Osservatorio Astronomico di Trieste, Istituto Nazionale di Astrofisica, I-34143 Trieste, Italy
[39] Department of Physics, University of Johannesburg, P.O. Box 524, Auckland Park 2006, South Africa
[40] Institut für Astro- und Teilchenphysik and Institut für Theoretische Physik, Leopold-Franzens-Universität Innsbruck, A-6020 Innsbruck, Austria
[41] NYCB Real-Time Computing Inc., Lattingtown, NY 11560-1025, USA
[42] Institució Catalana de Recerca i Estudis Avançats (ICREA), E-08010 Barcelona, Spain
[43] Dipartimento di Fisica, Università degli Studi di Perugia, I-06123 Perugia, Italy

[44] California State University, Los Angeles, Department of Physics and Astronomy, Los Angeles, CA 90032, USA
[45] Praxis Inc., Alexandria, VA 22303, resident at Naval Research Laboratory, Washington, DC 20375, USA

Abstract

We use joint observations by the *Swift* X-ray Telescope (XRT) and the *Fermi* Large Area Telescope (LAT) of gamma-ray burst (GRB) afterglows to investigate the nature of the long-lived high-energy emission observed by *Fermi* LAT. Joint broadband spectral modeling of XRT and LAT data reveals that LAT nondetections of bright X-ray afterglows are consistent with a cooling break in the inferred electron synchrotron spectrum below the LAT and/or XRT energy ranges. Such a break is sufficient to suppress the high-energy emission so as to be below the LAT detection threshold. By contrast, LAT-detected bursts are best fit by a synchrotron spectrum with a cooling break that lies either between or above the XRT and LAT energy ranges. We speculate that the primary difference between GRBs with LAT afterglow detections and the nondetected population may be in the type of circumstellar environment in which these bursts occur, with late-time LAT detections preferentially selecting GRBs that occur in low wind-like circumburst density profiles. Furthermore, we find no evidence of high-energy emission in the LAT-detected population significantly in excess of the flux expected from the electron synchrotron spectrum fit to the observed X-ray emission. The lack of excess emission at high energies could be due to a shocked external medium in which the energy density in the magnetic field is stronger than or comparable to that of the relativistic electrons behind the shock, precluding the production of a dominant synchrotron self-Compton (SSC) component in the LAT energy range. Alternatively, the peak of the SSC emission could be beyond the 0.1–100 GeV energy range considered for this analysis.

Key words: gamma-ray burst: general

1. Introduction

Joint observations by NASA's *Swift* and *Fermi* missions have led to a unique opportunity to study the broadband properties of gamma-ray bursts (GRBs) over an unprecedentedly broad energy range. The two missions have the combined capability of probing the emission from GRBs over 11 decades in energy, ranging from optical ($\sim$2 eV) to high-energy gamma rays ($>$300 GeV). After more than 7 yr of simultaneous operations, *Swift* and *Fermi* have detected thousands of GRBs, with over 100 of these bursts detected at energies greater than 30 MeV by the *Fermi* Large Area Telescope (LAT; Vianello et al. 2015).[47]

The properties of the high-energy emission observed by the LAT can differ considerably from the emission detected at keV and MeV energies by other instruments. While some bursts show evidence for emission in coincidence with activity at keV and MeV energies as observed by the *Swift* Burst Alert Telescope (BAT) and *Fermi* Gamma-ray Burst Monitor (GBM; Ackermann et al. 2010), others also exhibit high-energy emission that is temporally extended, lasting longer than the emission observed at lower energies (Ackermann et al. 2013a, 2014). There also appears in some cases to be a delay in the onset of the LAT-detected emission with respect to the emission observed at lower energies (Abdo et al. 2009a, 2009b; Ackermann et al. 2013b). The delayed onset and long-lived component of the LAT-detected emission suggest that GRB afterglows commonly observed in X-ray, optical, and radio wavelengths may also produce significant gamma-ray emission (Kumar & Barniol Duran 2009;

De Pasquale et al. 2010; Ghisellini et al. 2010; Razzaque et al. 2010). In this interpretation, the coincident emission detected by the LAT is thought to be an extension of the prompt emission spectrum commonly attributed to shocks internal to the relativistic outflow (Ackermann et al. 2010; Maxham et al. 2011; Yassine et al. 2017; Zhang et al. 2011), while the late-time emission is due to the high-energy extension of the electron synchrotron spectrum produced by the external forward shock associated with the GRB blast wave moving into the circumstellar environment.

Broadband fits to the simultaneous multiwavelength observations of GRB 110731A (Ackermann et al. 2013a) and GRB 130427A (Ackermann et al. 2014) show similar late-time spectral and temporal behavior, supporting such an external shock interpretation. Likewise, a stacking analysis of the LAT data of *Swift*-localized bursts that were not detected above 40 MeV has shown evidence for subthreshold emission on timescales that far exceed the typical duration of the prompt emission at keV energies (Beniamini et al. 2011; Ackermann et al. 2016). Furthermore, the strength of this high-energy subthreshold emission correlates directly with the X-ray brightness of the burst's afterglow emission, as measured by the *Swift* X-ray Telescope (XRT).

Despite the growing evidence for an external shock origin of the long-lived high-energy emission observed by the LAT, the fact remains that only $\sim$8% of the bursts detected at keV energies within the LAT field of view (FOV) have been detected above 40 MeV (Ackermann et al. 2013b). Therefore, although the signature of the afterglow emission at X-ray wavelengths is largely ubiquitous in GRBs observed by the XRT, the high-energy component is observed in only a small subset of these bursts. This has led to speculation that LAT-detected bursts may represent a unique population of GRBs, either probing a particular type of environment (Racusin et al. 2011; Beloborodov et al. 2014), the result of a unique set of afterglow conditions (Ghisellini et al. 2010), or the result of progenitors that produce a rare class of hyperenergetic GRBs (Cenko et al. 2011).

In this paper we attempt to address the conditions that are required to produce the late-time high-energy emission detected by the LAT through the use of broadband data collected by both *Swift* and *Fermi*. By examining joint XRT and LAT observations of 386 GRBs from 2008 August 4 to 2014 March 23, we can model the broadband spectra of the afterglow emission associated with LAT-detected and nondetected GRBs. This allows us to determine whether the relative sensitivities of the XRT and LAT are sufficient to account for the majority of LAT nondetections, or whether the LAT-detected bursts differ significantly in their afterglow properties from the general GRB population. A subset of these bursts is also subjected to detailed broadband spectral fitting of the simultaneous XRT and LAT data. From these spectral fits, we can determine whether the XRT and LAT data are consistent with being drawn from the same power-law segment (PLS) of an electron synchrotron spectrum, or if a break or suppression of the high-energy emission is required to explain the LAT nondetection. This analysis also allows us to place constraints on the existence of spectral components at high energies that are in excess of that predicted by the electron synchrotron model, such as external inverse Compton (EIC; Fan & Piran 2006; He et al. 2012; Beloborodov et al. 2014) and synchrotron self-Compton (SSC; Dermer et al. 2000; Sari & Esin 2001; Zhang & Mészáros 2001; Wang et al. 2013) contributions.

The paper is structured as follows: In Section 2, we review the characteristics of the *Fermi* LAT and *Swift* XRT instruments. In Section 3, we define the GRB samples considered in this work and outline the analysis performed in Section 4. We present the results in Section 5 and discuss the implications of our results in Section 6. Unless specified otherwise, all temporal and spectral indices are defined as $F_\nu \propto E^{-\beta} t^{-\alpha}$, where $\beta = \Gamma - 1$, with Γ the photon index.

2. Instrument Overview

2.1. Swift *BAT and* Swift *XRT*

Swift consists of the BAT (Barthelmy et al. 2005), the XRT (Burrows et al. 2005a), and the UltraViolet Optical Telescope (UVOT; Roming et al. 2005). The BAT is a wide-field, coded-mask gamma-ray telescope, covering an FOV of 1.4 sr and an imaging energy range of 15–150 keV. The instrument's coded mask allows for positional accuracy of 1–4 arcminutes within seconds of the burst trigger. The XRT is a grazing-incidence focusing X-ray telescope covering an energy range from 0.3 to 10 keV and providing a typical localization accuracy of ∼1–3′.

Swift operates autonomously in response to BAT triggers on new GRBs, automatically slewing to point the XRT at a new source within 1–2 minutes. Data are promptly downloaded, and localizations are made available from the narrow-field instruments within minutes (if detected). *Swift* then continues to follow up on GRBs, as they are viewable outside of observing constraints and the observatory is not in the South Atlantic Anomaly (SAA), for at least several hours after each burst, sometimes continuing for days, weeks, or even months if the burst is bright and of particular interest for follow-up.

2.2. Fermi *LAT*

Fermi consists of two scientific instruments, the GBM and the LAT. The LAT is a pair-conversion telescope comprising a 4×4 array of silicon strip trackers and cesium iodide (CsI) calorimeters covered by a segmented anti-coincidence detector to reject charged-particle background events. The LAT detects gamma rays in the energy range from 20 MeV to more than 300 GeV with an FOV of ∼2.4 sr, observing the entire sky every two orbits (∼3 hr) while in normal survey mode. The dead time per event of the LAT is nominally 26 μs, the shortness of which is crucial for observations of high-intensity transient events such as GRBs. The LAT triggers on many more background events than celestial gamma rays; therefore, onboard background rejection is supplemented on the ground using event class selections that are designed to facilitate study of the broad range of sources of interest (Atwood et al. 2009).

In normal *Fermi* operations, the GBM triggers on new GRBs approximately every 1–2 days. The LAT survey mode rocking profile is occasionally interrupted (approximately once per month) by GBM initiating an autonomous repoint request (ARR) due to high-peak flux or fluence, which has proven to be an effective proxy for bright LAT bursts. The ARR causes *Fermi* to reorient itself such that the GBM localization is placed at the center of the LAT FOV, where it remains for the next 2.5 hr, except when the GRB position is occulted by the Earth. Roughly 12 GRBs per year simultaneously trigger both the GBM and BAT, but due to extended high-energy γ-ray emission observed by the LAT in some bursts, a GRB does not necessarily need to be in the LAT FOV at the trigger time to be detected. In normal survey mode, the LAT observes the position of every GBM- and BAT-detected burst within 3 hr.

3. Sample Definition

We compiled a sample of all GRBs observed by the XRT between the beginning of *Fermi* science operations on 2008 August 4 and 2014 March 23. The majority of bursts in the sample were observed by LAT during its normal survey observations at some time after the BAT trigger and the start of XRT observations. A small number of bursts were not observed by the LAT owing to pointed observations at the time of the GRB trigger. For each burst observed by the LAT, we selected good time intervals (GTIs) during which the well-localized afterglow position was within 65° of the LAT z-axis (boresight) beginning after the start of the first XRT observation and ending up to 20 ks post trigger. The sensitivity of the LAT falls as a function of off-axis angle away from the instrument boresight; therefore, intervals during which the burst positions were >65° from the boresight were not considered for this analysis. Neither XRT nor LAT takes data during SAA passages; therefore, we also excluded intervals that occurred during these times. GRB positions that were at angles larger than 105° with respect to the zenith direction for *Fermi*, placing the burst near Earth's limb, were also excluded. Observations at such large zenith angles result in emission at the burst location that is dominated by γ-rays from Earth's limb produced by interactions of cosmic rays with Earth's atmosphere. The resulting sample includes a total of 1156 usable GTIs, for 386 GRBs.

4. Analysis

4.1. XRT

For each burst, we obtained the XRT count-rate light curves from the public XRT team repository hosted at the University of Leicester (Evans et al. 2007, 2009) and applied the de-absorbed counts-to-energy-flux conversion factor as determined by the automated late-time spectral fits to the XRT data.

Since the XRT coverage and the LAT GTIs may not always overlap, we fit the XRT light curves with a semi-automated light-curve fitting routine (Racusin et al. 2009, 2011, 2016) with power laws or broken power laws and Gaussian flares (when flaring episodes are present), in order to estimate the X-ray flux during XRT data gaps associated with periods of Earth occultation. We then use the afterglow's time-integrated photon index and associated error to convert the XRT energy flux light curve in the 0.3–10 keV energy range to an extrapolated energy flux light curve in the 0.1–100 GeV energy range. Note that by selecting only bursts for which there were LAT observations after the start of XRT observations, we avoid the highly uncertain activity of extrapolating both backward in time and to higher energies. Given the observations of both spectral and temporal variability in early afterglow light curves, including energetic X-ray flares and plateaus followed by sharp drops in flux, this decision avoids making any assumptions about the X-ray behavior prior to the onset of the XRT observations even though it excludes several well-observed LAT bursts for which subsequent XRT observations were made via *Swift* target-of-opportunity requests (e.g., GRB 080916C and GRB 090926A).

4.2. LAT

For each interval in which the GRB was in the LAT FOV, we calculate the 95% confidence level upper limits, or the observed energy flux with 68% errors, in the 0.1–100 GeV energy range for LAT nondetections and detections, respectively. We then compare these values to the expected energy flux in the 0.1–100 GeV energy range from the fit to the XRT data. The LAT flux estimates are obtained by performing an unbinned likelihood analysis using the standard analysis tools (ScienceTools version v10r01p0).[48] For this analysis, we used the "P8R2_SOURCE_V6" instrument response functions and selected "Source" class events from a 12° radius energy-independent region of interest (ROI) centered on the burst location. The size of the ROI is chosen to reflect the 95% containment radius of the LAT energy-dependent point-spread function (PSF) at 100 MeV. The "Source" event class was specifically optimized for the study of point-like sources, with stricter cuts against nonphoton background contamination relative to the "Transient" event class that is typically used to study GRBs on very short timescales (Ackermann et al. 2012a).

In standard unbinned likelihood fitting of individual sources, the observed distribution of counts for each burst is modeled as a point source using an energy-dependent LAT PSF and a power-law source spectrum with a normalization and photon index that are left as free parameters. For the purposes of comparing the XRT extrapolation to the LAT data, we fixed the model's photon index to match the value measured by the XRT. In addition to the point source, Galactic and isotropic background components are also included in the model, as well as all gamma-ray sources in the 3FGL catalog within a source region with a radius of 30° centered on each ROI (Acero et al. 2015). The Galactic component, *gll_iem_v06*, is a spatial and spectral template that accounts for interstellar diffuse gamma-ray emission from the Milky Way. The normalization of the Galactic component is kept fixed during the fit. The isotropic component, *iso_source_v06*, provides a spectral template to account for all remaining isotropic emission,

including contributions from both residual charged-particle backgrounds and the isotropic celestial gamma-ray emission. The normalization of the isotropic component is allowed to vary during the fit. Both the Galactic and isotropic templates are publicly available.[49]

We employ a likelihood ratio test (Neyman & Pearson 1928) to quantify whether there exists a significant excess of counts above the expected background. We form a test statistic (TS) that is twice the ratio of the likelihood evaluated at the best-fit parameters under a background-only, null hypothesis, i.e., a model that does not include a point-source component, to the likelihood evaluated at the best-fit model parameters when including a candidate point source at the center of the ROI (Mattox et al. 1996). According to Wilks's theorem (Wilks 1938), this ratio is distributed approximately as χ^2, so we choose to reject the null hypothesis when the test statistic is greater than TS = 16, roughly equivalent to a 4σ rejection criterion for a single degree of freedom. Using this test statistic as our detection criterion, we estimate the observed LAT flux for bursts with TS > 16 and use a profile likelihood method described in more detail in Ackermann et al. (2012b) to calculate upper limits for GRBs with TS < 15.

4.3. Joint XRT/LAT Spectral Fits

For bursts with time intervals during which the high-energy flux extrapolation of the XRT data is equivalent to, or exceeds, the measured LAT flux or upper limit for that period, we also performed joint spectral fits to the XRT and LAT data to investigate the underlying shape of the spectral energy distribution (SED). To simplify the analysis, we only considered intervals with contemporaneous XRT and LAT data. We refer to this subsample of GTIs as our "spectroscopic" sample.

For these fits, the *Swift* XRT data, including relevant calibration and response files, were retrieved from the HEASARC archive[50] and processed with the standard *Swift* analysis software (v3.8) included in NASA's HEASOFT software (v6.11). We use *gtbin* to generate the count spectrum of the observed LAT signal and *gtbkg* to extract the associated background by computing the predicted counts from all the components of the best-fit likelihood model except the point source associated with the GRB. The LAT instrument response for each interval was computed using *gtrspgen*.

The spectral fits were performed using the XSPEC version 12.7.0 (Arnaud 1996). Because the number of counts in the LAT energy bins is often in the Poisson regime, we use the PG statistic from XSPEC, since the standard χ^2 statistic is not a reliable estimator of significance for low counts. For bursts with no detectable emission, the count spectra associated with the modeled signal cannot exceed the background spectra. XSPEC takes this into account by constraining the best-fit model from overpredicting the signal counts in the LAT energy range. The resulting flux upper limits from these background-only intervals help constrain the hardness of the spectral model.

For each time interval, we fit two functional forms to the XRT and LAT data: a single power-law (PL) and a broken power-law (BPL) model. Each form is multiplied by models for both fixed Galactic (phabs) and free intrinsic host (zphabs for bursts with known redshift, phabs otherwise) photoelectric
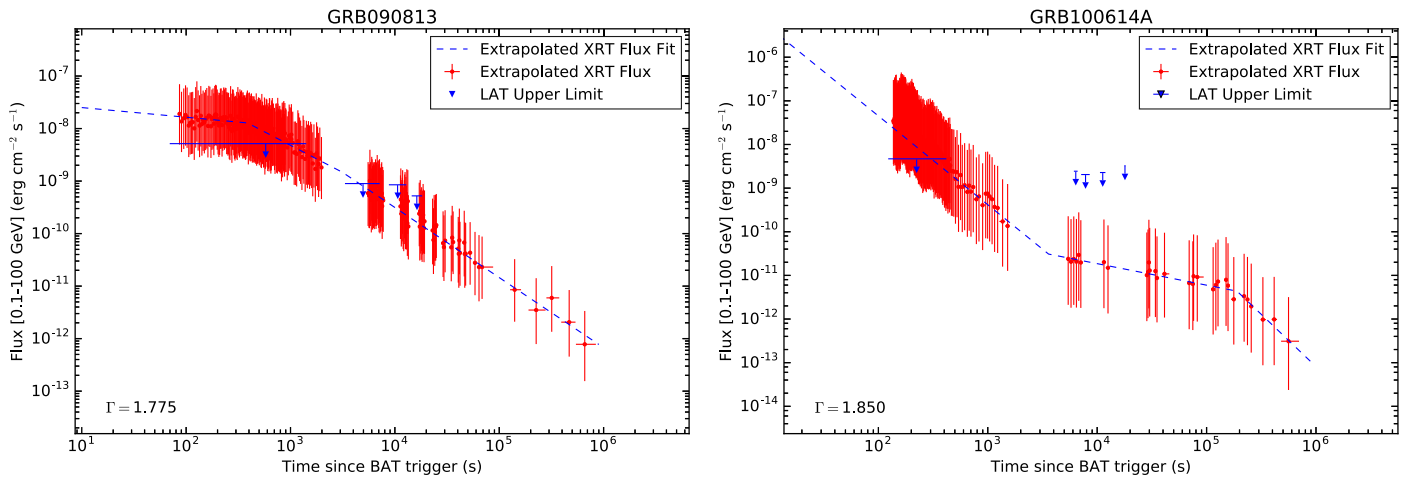

Figure 1. Examples of the comparison between the XRT-extrapolated flux and the LAT observations in the 0.1–100 GeV energy range for GRB 090813 and GRB 100614A. The Γ listed in the lower left corner indicates the time-averaged X-ray photon index used in the extrapolation. The blue dashed line represents the best-fit power-law segments to the X-ray afterglow flux. Neither burst was detected by the LAT despite both exhibiting bright X-ray afterglows and relatively hard photon indices and being well observed by the LAT soon after the onset of the afterglow decay.

absorption and a free cross-calibration constant. Assuming that any break in the spectrum between the XRT and LAT regimes at late times would be associated with the synchrotron cooling frequency, i.e., the frequency at which an electron's cooling time equals the dynamical time of the system, we require the two power-law indices in the BPL model to differ by $\Delta\Gamma = 0.5$ in accordance with the theoretical expectation for electron synchrotron radiation from a forward shock (Granot & Sari 2002).

We perform a nested model comparison in order to determine whether the additional degrees of freedom in the BPL model are warranted over a simpler PL model. Assuming that there are n_{alt} additional free parameters under the alternative model, then the alternative model is statistically preferred at a confidence level according to the difference in the PG statistic, hereafter referred to as ΔStat, between the two fits, which is expected to follow a χ^2 distribution for n_{alt} degrees of freedom in the large sample limit. Requiring that the two power-law indices in the BPL model differ by $\Delta\Gamma = 0.5$ results in a single extra degree of freedom (i.e., the break energy) compared to the PL null hypothesis. Therefore, according to the χ^2 cumulative distribution function, a value of ΔStat > 9 would represent a $>3\sigma$ improvement in the fit. We adopt this criterion as the threshold for a statistical preference for a break in the high-energy spectrum.

5. Results

5.1. XRT Flux Extrapolations

Examples of comparisons between the XRT fluxes extrapolated into the 0.1–100 GeV energy range and the LAT observations for GRB 090813 and GRB 100614A are shown in Figure 1. The error bars on this XRT-extrapolated LAT-band flux (hereafter referred to as the XRT-extrapolated flux) take into account the propagation of uncertainty of both the X-ray flux and photon index into the LAT energy range. Both bursts shown in Figure 1 exhibit bright X-ray afterglows and relatively hard photon indices and were well observed by the LAT soon after the onset of the afterglow decay. Neither burst was detected by the LAT, and the estimated upper limits for the energy flux in the 0.1–100 GeV energy range are above or are

consistent with the expected flux given the extrapolation of the XRT spectrum.

The results of performing the same analysis on all 1156 GTIs in our sample are shown in Figure 2. The plot shows the measured LAT flux, or upper limit, versus the XRT-extrapolated flux for a given interval when the burst location was within the LAT FOV. The gold stars represent the LAT detections in our sample, which consist of 14 GTIs for 11 GRBs. We note that all but one of these detections were announced via the Gamma-ray Coordinates Network (GCN),[51] the two exceptions being GRB 081203A and GRB 120729A, both of which were found through this analysis. Both these bursts are discussed in greater detail in the second *Fermi* LAT GRB catalog (The LAT Collaboration 2018, in preparation).

For 91% of the intervals examined (1055 GTIs), the XRT-extrapolated flux in the LAT energy range fell below the LAT upper limits (i.e., to the left of the equivalency line) and therefore were consistent with the LAT nondetections. The extrapolated fluxes for an additional ∼7% (84 GTIs) were above the LAT upper limits (i.e., to the right of the equivalency line). Interestingly, the flux measurements for all of the LAT detections in our sample either were consistent with the XRT extrapolation (4 GTIs) or fell below it (10 GTIs). None of the LAT detections showed evidence of emission significantly in excess of the flux expected from the extrapolation of the XRT observations.

We examined the X-ray properties of the afterglows during these intervals in Figure 3, where we plot the X-ray energy flux as measured by the XRT in the 0.3–10 keV energy range versus the associated photon index Γ_{XRT}. The intervals with afterglow emission that would be expected to produce high-energy emission in excess of the LAT sensitivity tend to be spectrally hard, with $\Gamma_{XRT} \lesssim 2$. They are also drawn from a very wide range of fluxes. The LAT detections, on the other hand, are drawn exclusively from afterglows that exhibited bright and hard emission, with criteria roughly fulfilling $\Gamma_{XRT} \lesssim 2$ and $F_{XRT} \gtrsim 10^{-10}$ erg cm^{-2} s^{-1} shown as dashed green lines. The red points that occupy this quadrant of the plot did not have sufficiently deep upper limits for the expected high-energy flux
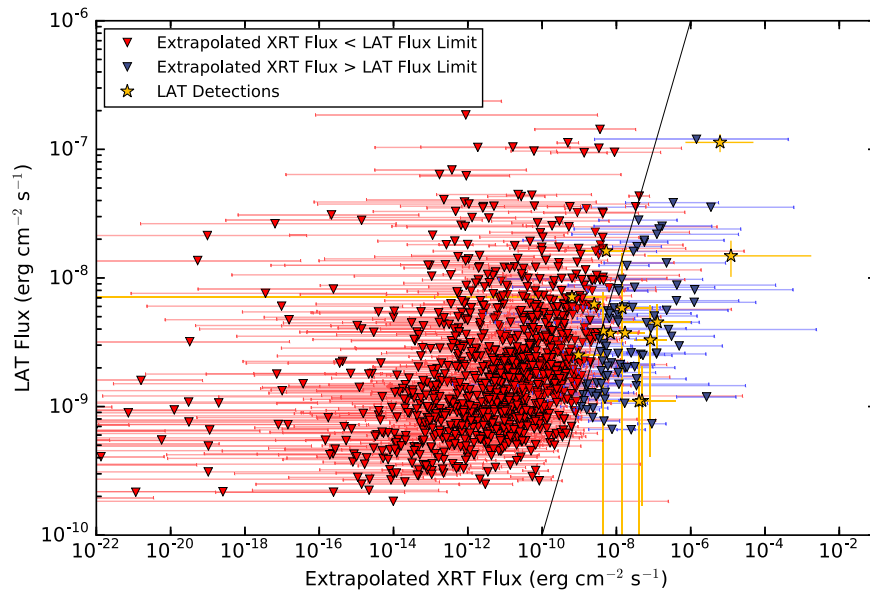

Figure 2. Measured LAT flux (yellow stars), or upper limit (downward-pointing triangles), vs. the XRT-extrapolated flux for a given interval when the burst location was within the LAT FOV. The black line demarcates the equivalency. The blue and red colors of the downward-pointing triangles represent intervals when the extrapolated flux fell above and below the LAT flux measurements, respectively. The gold stars represent the LAT detections in our sample.
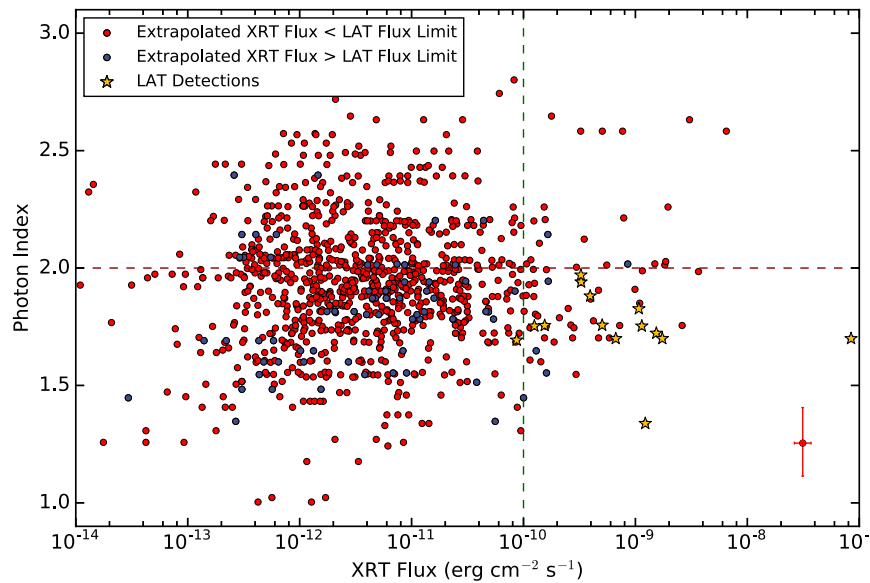

Figure 3. Time-averaged photon index Γ vs. the X-ray energy flux as measured by the XRT in the 0.3–10 keV energy range. The blue and red symbols represent intervals when the extrapolated flux fell above and below the LAT flux measurements, respectively, and the gold stars represent the LAT detections in our sample. The typical error bar is shown in the bottom right corner, and the vertical and horizontal dashed lines separate the plot into soft/hard and dim/bright quadrants.

to exceed the LAT sensitivity, so their nondetections are consistent with the LAT observations. The blue points, on the other hand, have deeper LAT upper limits, making their expected high-energy emission inconsistent with the LAT observations.

We examine the properties of these afterglow intervals after folding in the LAT sensitivity in Figure 4, where we display the time-averaged photon indices for the afterglows, as measured by XRT, versus the ratio of the XRT-extrapolated fluxes in the LAT energy range to the LAT upper limits (or measured fluxes for detections). The colors of the symbols now represent the XRT energy fluxes measured during the geometric mean of the afterglow interval. The geometric mean is defined as the square root of the product of the interval start and end times. The green dashed line represents the line of equivalency between the

measured LAT flux (or upper limit) and the XRT-extrapolated flux. Bursts that fall to the right have X-ray extrapolations that are consistent with the LAT sensitivity, whereas bursts that fall to the left have X-ray extrapolations that exceed the LAT flux measurements. By construction, all of the blue data points in Figures 2 and 3 lie to the right of the green dashed line. Again, a general trend is evident wherein the bursts with the hardest afterglow spectra and highest observed XRT fluxes during the intervals in question are the bursts that result in X-ray extrapolations that either exceed the LAT upper limits or result in LAT detections.

Figure 5 displays the same results, but now showing the ratio of the XRT-extrapolated flux to the measured LAT flux (or upper limit) versus the geometric mean of the temporal interval in which the burst position was within the LAT FOV. The
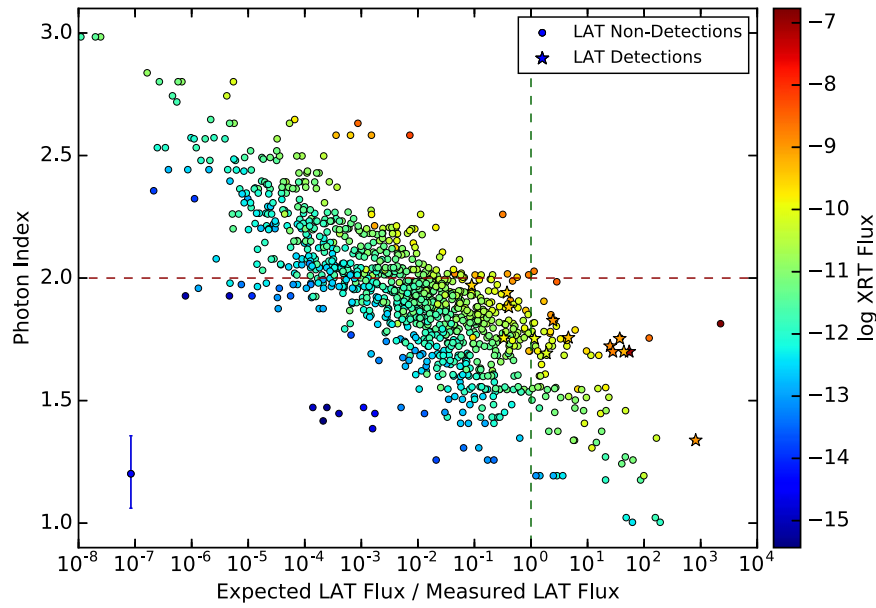
6

Figure 4. Time-averaged afterglow photon index, as measured by XRT, vs. the ratio of the XRT-extrapolated flux in the LAT energy range to the LAT upper limit (or measured flux in the case of a detection). The colors of the symbols show the XRT energy flux measured during the geometric mean of the afterglow interval, where the geometric mean is defined as the square root of the product of the interval start and end times. The green line represents the line of equivalency between the measured LAT flux (or upper limit) and the XRT-extrapolated flux. The typical error bar is shown in the bottom left corner, and the red dashed lines delineate the soft/hard populations, and the green dashed line marks the line of equality between the expected and measured LAT flux.
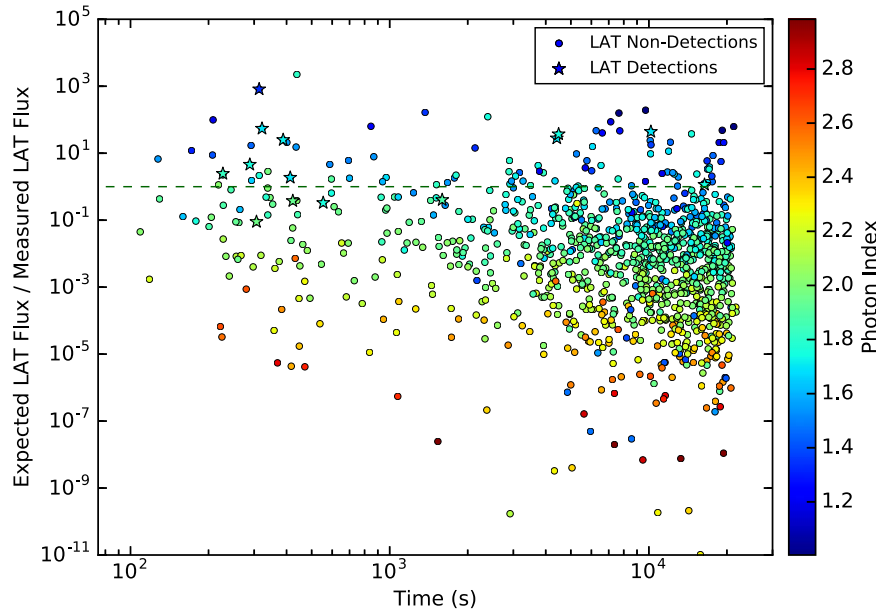

Figure 5. Ratio of the XRT-extrapolated flux to the measured LAT flux (or upper limit) vs. the geometric mean of the interval in which the burst position was within the LAT FOV. The colors of the symbols represent the time-averaged photon index as measured by spectral fits to the late-time XRT data, and the stars represent the LAT detections. The vertical green dashed line represents the line of equality between the measured LAT flux (or upper limit) and the XRT-extrapolated flux.

colors of the symbols represent the time-averaged photon index as measured by spectral fits to the late-time XRT data. The stars again represent the LAT detections. Again, we see a general trend of bursts with harder afterglow spectra tending to predict high-energy emission in excess of the LAT sensitivity. Although X-ray brightness correlates strongly with the time of observation, Figure 5 demonstrates that many afterglows remain spectrally hard to late times, resulting in afterglow emission that exceeds the LAT sensitivity thousands of seconds

after trigger. Likewise, the LAT detections appear in both early- and late-time observations.

In order to understand what differentiates the afterglow intervals that have expected high-energy emission that is inconsistent with the LAT observations from those with LAT detections, we selected all intervals to the right of the line of equivalency in Figure 2 (i.e., the blue data points), as well as all of the LAT-detected bursts (yellow data points), for which simultaneous XRT and LAT data exist. A total of 64 GTIs for
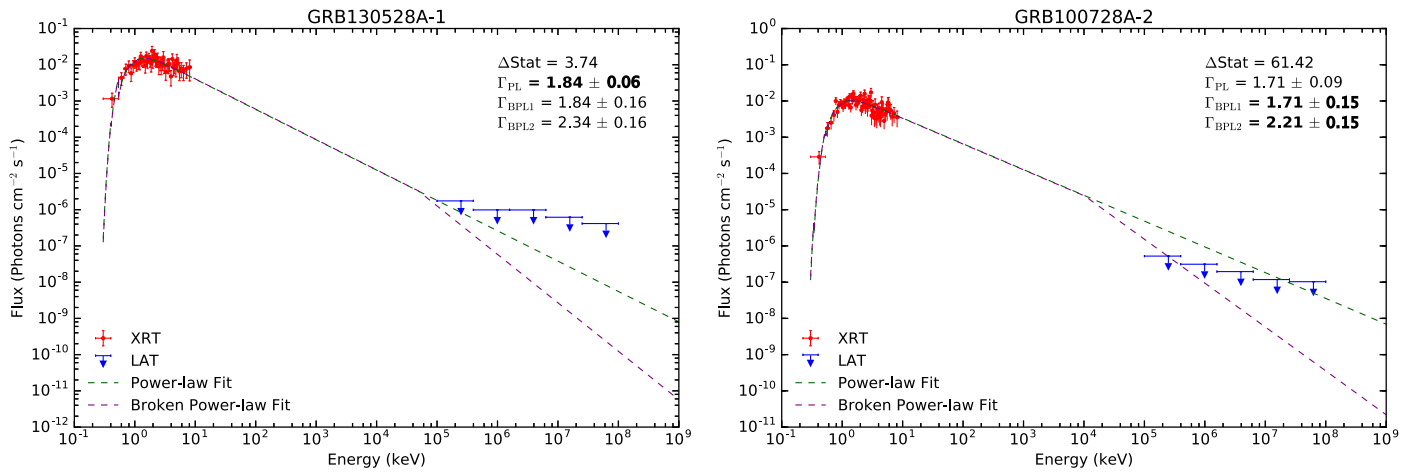
Figure 6. Joint spectroscopic fits performed using the contemporaneous XRT and LAT data for GRB 130528A and the second interval of GRB 100728A. The measured XRT spectrum in the 0.3–10 keV energy range is shown in red, while the LAT upper limits (95% confidence level) are shown as blue downward-pointing arrows. The green and purple dashed lines represent fits to the data using the single and broken power-law models. The photon indices from the statistically preferred fit are shown in bold.

Table 1
Summary of the Median Best-fit Parameters for the Joint XRT/LAT Spectral Fits Outlined in Sections 5.2 and 5.3

Sample	Best Fit	GTIs	$\Gamma_{\rm XRT}$	$\Gamma_{\rm PL}$	$\Gamma_{\rm BPL1}$	$\Gamma_{\rm BPL2}$
LAT nondetections	PL	31 (58%)	1.68 ± 0.21	1.98 ± 0.16	⋯	⋯
LAT nondetections	BPL	21 (40%)	1.72 ± 0.21	⋯	1.60 ± 0.13	2.10
LAT detections	PL	6 (55%)	1.76 ± 0.21	1.77 ± 0.04	⋯	⋯
LAT detections	BPL	5 (45%)	1.70 ± 0.17	⋯	1.72 ± 0.10	2.22

52 bursts fulfill these criteria and form the spectroscopic sample for which we performed additional joint spectral fits, described in the next section.

5.2. Joint XRT/LAT Spectroscopic Fits

Two examples of the joint spectroscopic fits performed using the contemporaneous XRT and LAT data for GRB 130528A and GRB 100728A are shown in Figure 6. The measured XRT spectrum in the 0.3–10 keV energy range is shown in red, while the LAT upper limits (95% confidence level) are shown as blue downward-pointing arrows. The green and purple dashed lines represent fits to the data using the single and broken power-law models described in Section 4.3. Neither GRB 130528A nor GRB 100728A was detected by the LAT during the selected intervals (GRB 100728A was detected at an earlier time), so upper limits are shown for emission in the 0.1–100 GeV energy range. Combined with the XRT data, these limits constrain the broadband spectral shape of the afterglow emission from these two bursts. In the case of GRB 130528A, a single power law covering eight orders of magnitude in energy is consistent with both the XRT and LAT data, whereas a broken power law is statistically preferred in GRB 100728A, with an $\sim 8\sigma$ (ΔStat = 64.21) improvement in the fit over a single power law.

Of the 64 GTIs in our spectroscopic sample, a total of 52 intervals yielded no LAT-detected emission. Of these 52 GTIs, 31 (60%) have simultaneous XRT and LAT data that are consistent with being drawn from a spectral distribution that can be represented as a single power law. An additional 21 GTIs (40%) show a statistical preference, at greater than 3σ significance, for a spectral break between the XRT and LAT data. In all but one case, the LAT data can be accommodated by either a power law or a broken power law, with a photon

index change of $\Delta\Gamma = 0.5$, connecting the contemporaneous XRT and LAT observations.

A median photon index of $\Gamma_{\rm PL} = 1.98 \pm 0.16$ was measured for the 31 GTIs for which a single power law was adequate to describe both the XRT and LAT data, where we have adopted the standard deviation of the sample as the error on the median. This is in contrast to the median photon index of $\Gamma_{\rm XRT} = 1.68 \pm 0.21$ for this sample when measured from the XRT data alone. Therefore, adding the LAT data to the spectral fit softens the estimated spectral shape for these bursts. For the bursts that show a preference for a break in their broadband afterglow spectra, we find median XRT and LAT photon indices of $\Gamma_{\rm BPL1} = 1.60 \pm 0.13$ and $\Gamma_{\rm BPL2} = 2.10$, where the post-break photon index is fixed to $\Gamma_{\rm BPL2} = \Gamma_{\rm BPL1} + 0.5$. This is compared to the median photon index of $\Gamma_{\rm XRT} = 1.72 \pm 0.21$ for this sample when estimated from the XRT data alone. The median spectral fit results are summarized in Table 1.

5.3. LAT Detections

The temporal and spectral fits for the 11 LAT-detected bursts with contemporaneous XRT and LAT data in our spectroscopic sample are shown in Figure 7. The spectral fits were performed using data extracted from the first detected interval for each burst. Of the 11 bursts analyzed, 5 show a preference for a break in their broadband spectrum between the XRT and LAT, with the remaining 6 being consistent with a single power law from the X-ray to gamma-ray regimes. As mentioned in Section 5.1, the flux measurements for all of the LAT detections either were consistent with the XRT extrapolation or fell below it, which is confirmed by the joint spectral fits. The broadband X-ray and gamma-ray spectral data for the LAT detections are all well fit by either a power-law or a broken
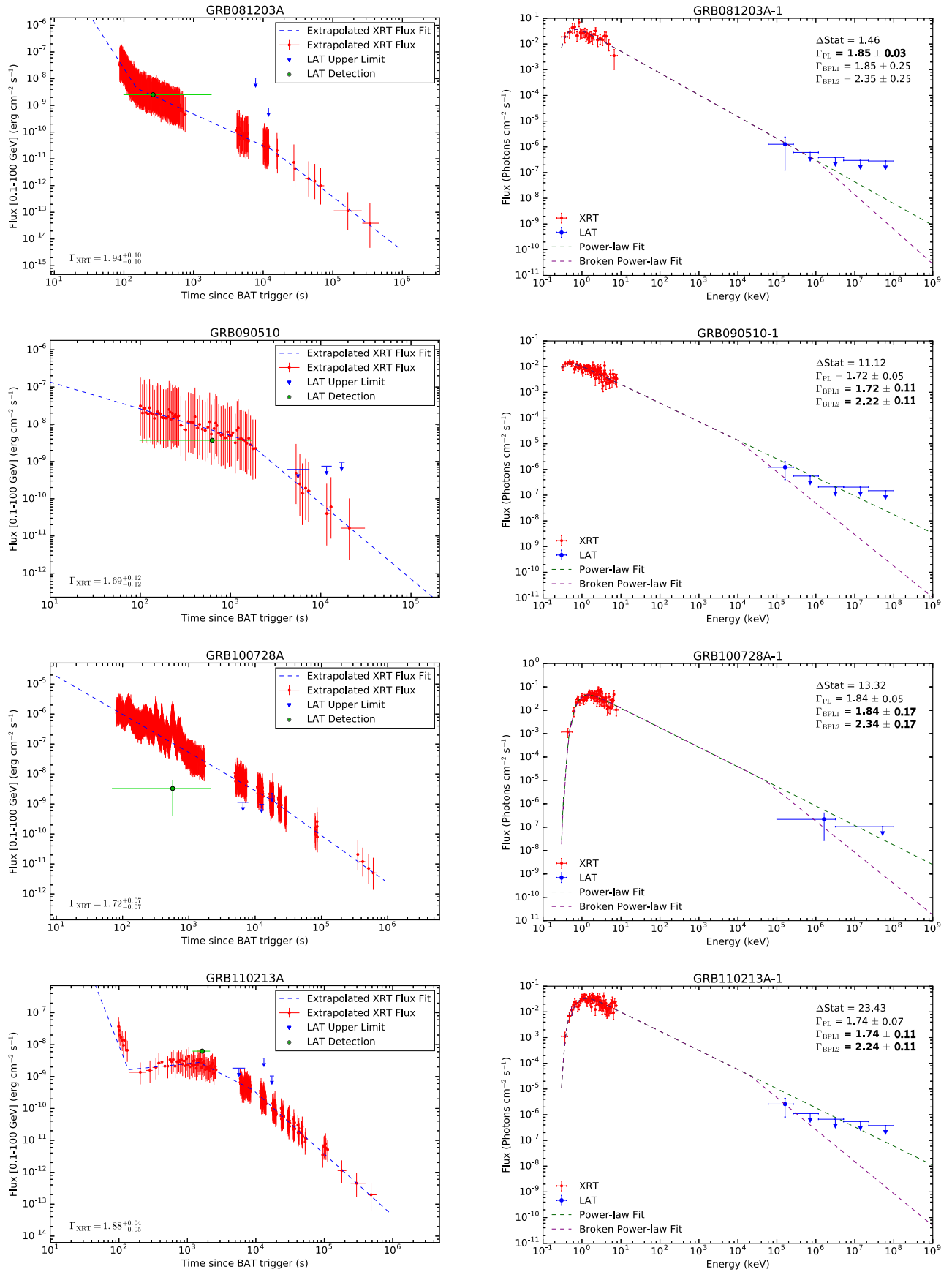
Figure 7. Temporal and spectral fits (left and right panels) for the 11 LAT-detected bursts with simultaneous XRT and LAT observations in our sample. The photon indices Γ_{XRT} listed in the temporal plots are derived from fits to only the time-integrated XRT data, whereas the photon indices listed on the spectral fits are obtained through the joint fits of both the XRT and LAT data. The numeric suffix in the title of the spectral plots indicates the temporal interval from which these data were extracted.
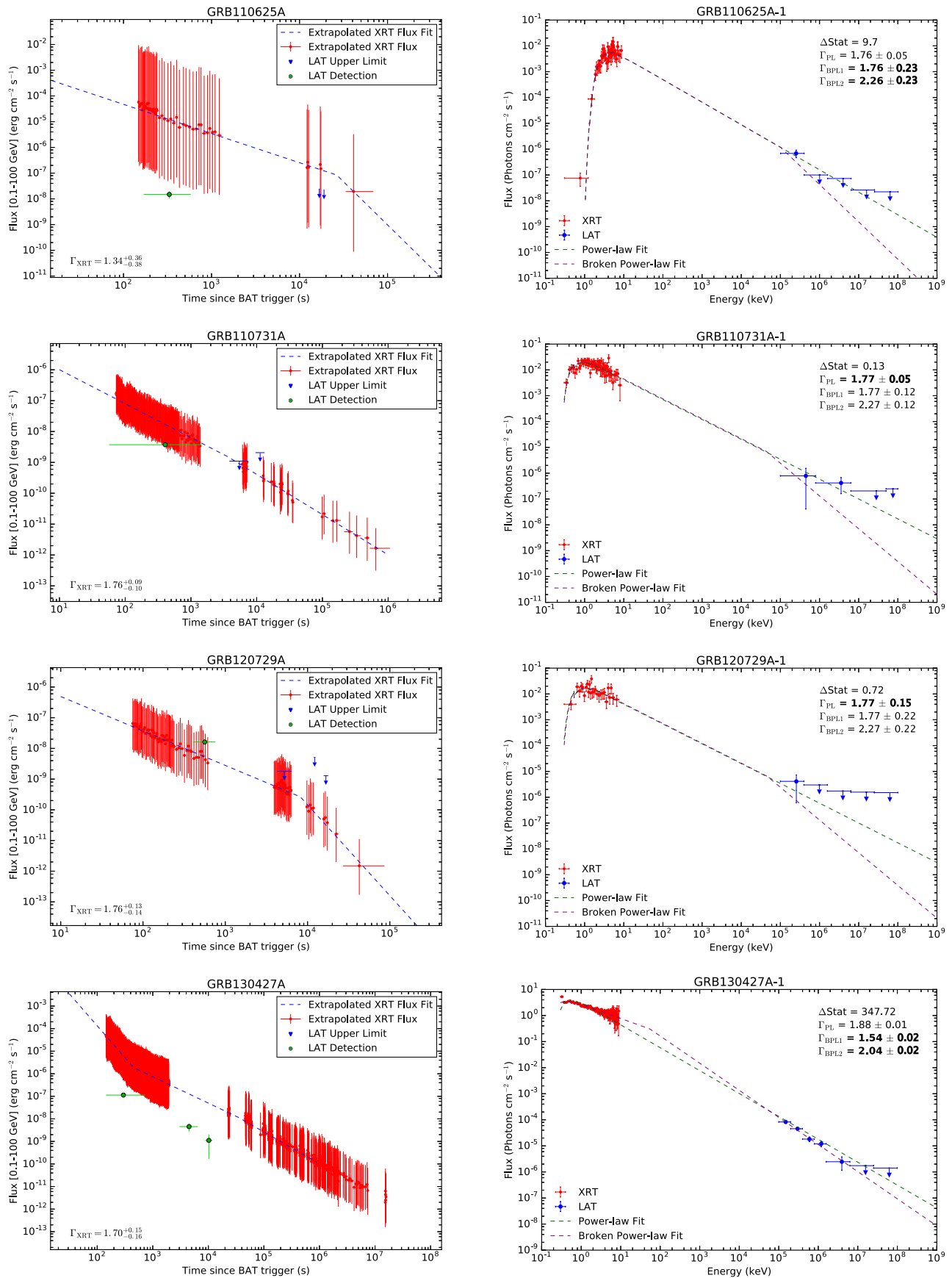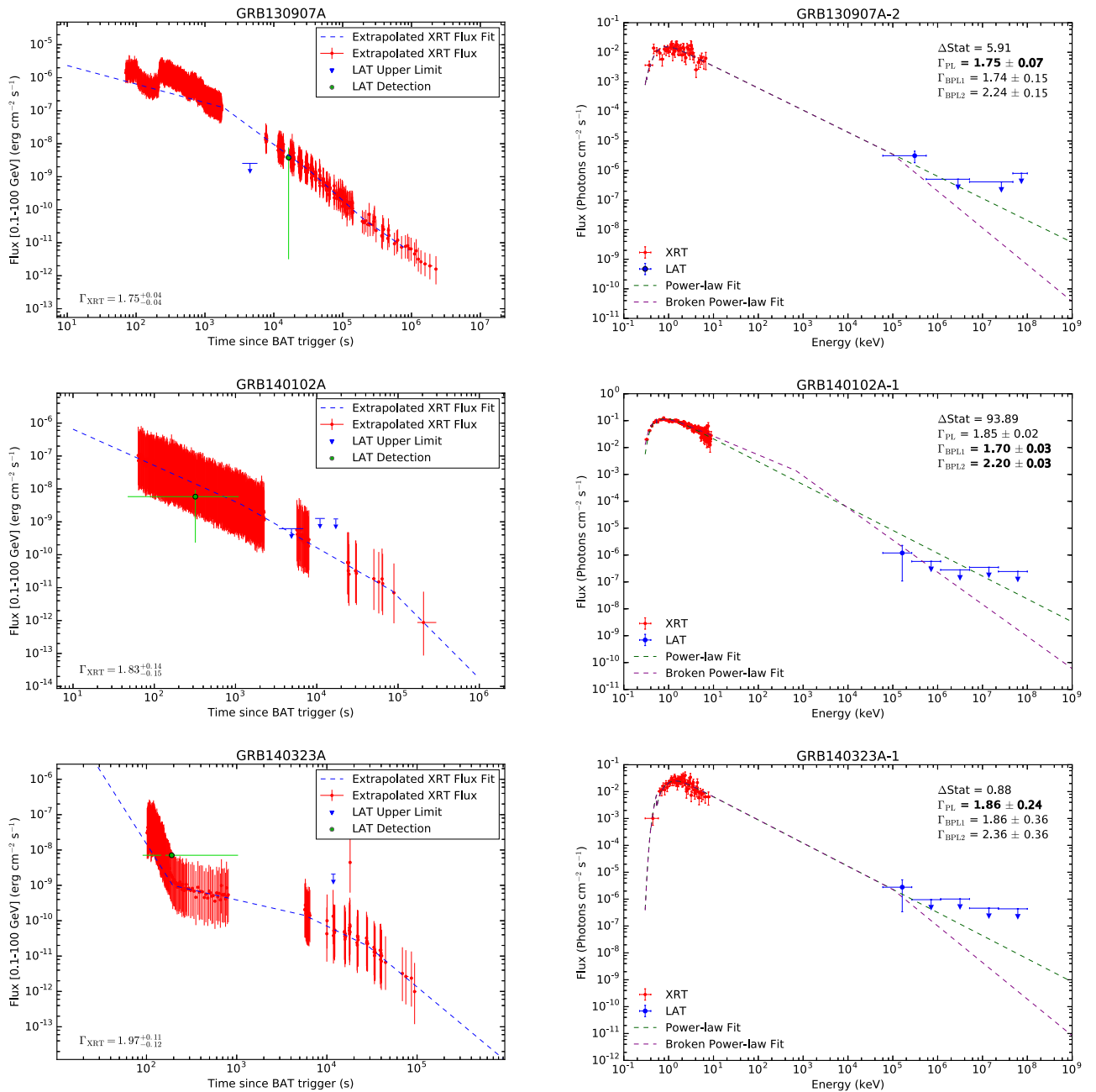
Figure 7. (Continued.)

Figure 7. (Continued.)

power-law model and show no evidence of high-energy emission significantly in excess of the flux expected from the XRT observations.

All of the LAT-detected bursts in our sample exhibit bright X-ray afterglows with relatively hard X-ray photon indices (i.e., $\Gamma_{XRT} < 2$). A median photon index of $\Gamma_{PL} = 1.77 \pm 0.04$ was measured for the six GTIs for which a single power law was adequate to describe both the XRT and LAT data. Unlike for the LAT nondetected bursts, this value is consistent with the median photon index of $\Gamma_{XRT} = 1.76 \pm 0.21$ for this sample when estimated from the XRT data alone. For the bursts that show a preference for a break in their broadband afterglow spectrum, we find median XRT and LAT photon indices of $\Gamma_{BPL1} = 1.72 \pm 0.10$ and

$\Gamma_{BPL2} = 2.22$. The pre-break photon index is again consistent with the value estimated from the XRT data alone of $\Gamma_{XRT} = 1.70 \pm 0.17$ for this sample. The fit parameters for each individual LAT-detected burst are displayed in Table 2.

Our analysis reveals that a single power law is capable of explaining the broadband emission from GRB 110731A, whereas the emission observed from GRB 130427A and GRB 090510 requires a spectral break between the X-ray and gamma-ray regimes. These results are consistent with those previously reported by Ackermann et al. (2013a), Kouveliotou et al. (2013), and De Pasquale et al. (2010), respectively. Conversely, we find that a spectral break is statistically preferred for GRB 100728A, contrary to the findings of Abdo et al. (2011). In the latter case, the differing results can likely be

Table 2
Summary of the Best-fit Spectral Parameters for the LAT-detected Population in Our Sample

GRB	Γ_{XRT}	Γ_{LAT}	Best Fit	ΔStat	Γ_{PL}	Γ_{BPL1}	Γ_{BPL2}	E_b (keV)
081203A	$1.94^{+0.10}_{-0.10}$	2.18 ± 0.36	PL	1.5	1.85 ± 0.03	1.85 ± 0.25	2.35	⋯
090510A	$1.69^{+0.12}_{-0.12}$	2.44 ± 0.55	BPL	11.1	1.72 ± 0.05	1.72 ± 0.11	2.22	9958 ± 968
100728A	$1.72^{+0.07}_{-0.07}$	1.70 ± 0.22	BPL	13.3	1.84 ± 0.05	1.84 ± 0.17	2.34	9568 ± 1045
110213A	$1.88^{+0.04}_{-0.05}$	1.60 ± 0.36	BPL	23.4	1.74 ± 0.07	1.74 ± 0.11	2.24	10000 ± 946
110625A	$1.34^{+0.36}_{-0.38}$	2.49 ± 0.22	BPL	9.7	1.76 ± 0.05	1.76 ± 0.23	2.26	7125 ± 1060
110731A	$1.76^{+0.09}_{-0.10}$	1.69 ± 0.37	PL	0.1	1.77 ± 0.05	1.77 ± 0.12	2.27	⋯
120729A	$1.76^{+0.13}_{-0.14}$	1.77 ± 0.35	PL	0.7	1.77 ± 0.15	1.77 ± 0.22	2.27	⋯
130427A	$1.70^{+0.15}_{-0.16}$	2.06 ± 0.07	BPL	347.7	1.88 ± 0.01	1.54 ± 0.02	2.04	54 ± 18
130907A	$1.75^{+0.04}_{-0.04}$	2.05 ± 0.35	PL	5.9	1.75 ± 0.07	1.74 ± 0.15	2.24	⋯
140102A	$1.83^{+0.14}_{-0.15}$	1.53 ± 0.31	BPL	93.9	1.85 ± 0.02	1.70 ± 0.03	2.20	681 ± 16
140323A	$1.97^{+0.11}_{-0.12}$	1.86 ± 0.42	PL	0.9	1.86 ± 0.24	1.86 ± 0.36	2.36	⋯

Note. Γ_{XRT} and Γ_{LAT} are the photon indices obtained from fitting the XRT and LAT GTIs separately, whereas Γ_{PL}, Γ_{BPL1}, and Γ_{BPL2} are the photon indices obtained through the joint XRT and LAT fits to power-law (PL) and broken power-law (BPL) models, respectively. The post-break photon index in the BPL model is fixed to $\Gamma_{\mathrm{BPL2}} = \Gamma_{\mathrm{BPL1}} + 0.5$. A BPL model is statistically preferred at $>3\sigma$ over a simpler PL model when ΔStat > 9.

attributed to the greater sensitivity of the Pass 8[52] data selection used in this work, compared to the Pass 7 data selection used in previous papers.

6. Discussion

The results presented in Section 5.1 reveal that a majority of bursts that are detected by *Swift* XRT do not have sufficiently bright afterglows and/or hard spectra to be detected by *Fermi* LAT. Of the 1156 intervals that we analyzed for this study, we found that only a small subset exhibited afterglow emission that could exceed the LAT detection threshold when extrapolated to the 0.1–100 GeV energy range. This finding illustrates that the late-time detection of afterglow emission by the LAT at high energies is relatively uncommon, despite nearly every *Swift*-detected GRB being within the LAT FOV at some point before the end of XRT observations. The bursts that do result in late-time LAT detections exclusively have afterglow intervals with emission brighter than $F_{\mathrm{XRT}} \gtrsim 10^{-10}\,\mathrm{erg\,cm^{-2}\,s^{-1}}$ and harder than $\Gamma_{\mathrm{XRT}} \lesssim 2$.

We performed joint spectral fits of simultaneous XRT and LAT data for 52 GTIs for which no emission was detected by the LAT, but for which their XRT-derived afterglow spectra were sufficiently bright and hard that they exceed the LAT upper limits. These fits reveal that a majority of these cases (58%) can be explained by an afterglow spectrum with a slightly softer photon index when constrained by both the XRT and LAT data, compared to the photon index derived by fits to the XRT data alone. The remaining LAT nondetections required a break in their afterglow spectra between the XRT and LAT energy ranges, consistent with a cooling break expected in the high-energy regime of electron synchrotron emission from a relativistic blast wave expanding into an external medium.

Of the 11 LAT-detected bursts in our sample, we find that the measured flux in the 0.1–100 GeV energy range either is consistent with or falls below the flux expected at these energies from an extrapolation of their afterglow spectra as derived from simultaneous XRT observations. These results are confirmed by joint spectral fits of XRT and LAT data for these bursts, which show that the broadband X-ray and gamma-ray

data are well fit by either a simple power-law or a broken power-law model that is consistent with a cooling break between the energy ranges of the two instruments. As a result, we find no evidence of high-energy emission significantly in excess of the flux expected from the spectrum predicted by the electron synchrotron model.

6.1. On the Nature of the LAT-detected Population

An examination of the photon indices derived from the joint spectral fits for the LAT-detected and nondetected bursts suggests a difference between these two populations. For the LAT nondetected bursts, the median photon index of the spectral component connecting the XRT and LAT data is $\Gamma_{\mathrm{PL}} = 1.98 \pm 0.16$. This value is consistent with the canonical value of $\Gamma \sim 2$ expected from the high-energy component of the electron synchrotron spectrum for both the slow- and fast-cooling scenarios, for an assumed power-law electron energy distribution of $p = 2$. Likewise, the LAT nondetected bursts for which a break between the XRT and LAT was required have median pre- and post-break power-law indices of $\Gamma_{\mathrm{BPL1}} = 1.6 \pm 0.13$ and $\Gamma_{\mathrm{BPL2}} = 2.1$, again consistent with the expected $\Gamma \sim 2$ post-break value. This indicates that the cooling break of the synchrotron spectrum lies either below or between the XRT and LAT energy ranges for the LAT nondetections for which we performed joint spectral fits.

By contrast, the LAT-detected bursts with broadband XRT and LAT data that are best fit by a single power-law component yield a harder median photon index of $\Gamma_{\mathrm{PL}} = 1.77 \pm 0.04$. The LAT-detected bursts for which a break between the XRT and LAT was required have median values of the pre- and post-break power-law indices $\Gamma_{\mathrm{BPL1}} = 1.72 \pm 0.10$ and $\Gamma_{\mathrm{BPL2}} = 2.22$, respectively. The cooling break of the synchrotron spectrum for these bursts appears to occur either between or above the XRT and LAT energy ranges for a majority of the LAT-detected bursts. Not a single LAT-detected burst examined in our analysis has an X-ray photon index that is consistent with the canonical $\Gamma \sim 2$ value expected for the highest-energy component predicted by an electron synchrotron spectrum in either a slow- or fast-cooling regime.

The trend of LAT-detected bursts being spectrally harder in X-ray than their nondetected counterparts can be seen in an examination of the afterglow properties of all LAT-detected
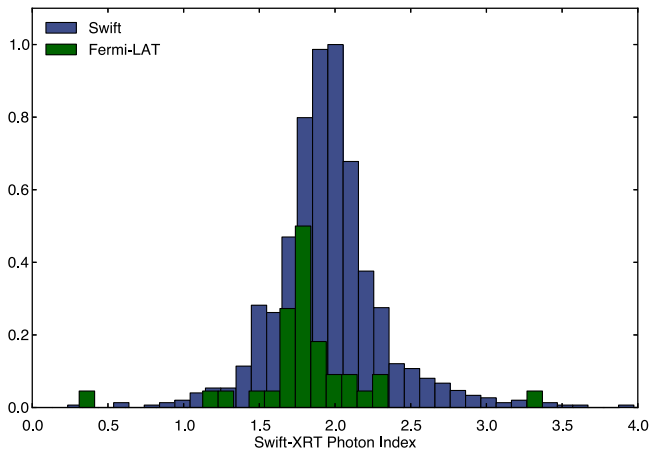
Figure 8. Comparison of the X-ray photon index distribution for all *Swift* XRT-detected GRBs (blue) and those detected by the LAT (green), for which *Swift* XRT observations exist.

bursts observed by the XRT. Figure 8 compares the photon index distributions of all LAT-detected GRBs for which *Swift* XRT observations exist. A two-sided K-S test yields a *p*-value of 0.0146, rejecting the hypothesis that the two samples are drawn from the same distribution. Here we have dropped the requirement that the LAT detection occurred after the start of the first XRT observations, because we are examining the properties of the afterglows of all LAT-detected bursts and and are not making a joint analysis between the two instruments. This allows us to include bursts such as GRB 080916C and GRB 090323A, which were detected by the LAT, but for which XRT observations began after the LAT detections, and therefore they were excluded from our previous analysis. The X-ray photon index distribution for all GRB afterglows observed by the XRT peaks at $\Gamma_{\rm XRT} \sim 2$, indicating that the observed emission is consistent with the highest-energy component predicted by an electron synchrotron spectrum in either the slow- or fast-cooling regimes. By contrast, the X-ray photon index distribution for LAT-detected bursts peaks at a harder value of $\Gamma_{\rm XRT} \sim 1.8$, again suggesting that the synchrotron spectrum's cooling break lies either between or above the XRT and LAT energy ranges for a majority of the LAT-detected bursts.

A potentially important effect that we note is that the cooling break frequency ($\nu_{\rm c}$) in the afterglow synchrotron spectrum is expected to be very smooth and possibly extend over $\sim$2–3 decades in photon energy (Granot & Sari 2002). Therefore, (i) in some cases $\nu_{\rm c}$ might be near the XRT energy range, in which case $\Gamma_{\rm XRT} > \Gamma_1$ will be inferred, with the spectral index measured by the LAT being $\Gamma_{\rm LAT} < \Gamma_2$, resulting in a measured (or effective) spectral break $\Delta\Gamma_{\rm eff}$ that is less than the theoretical prediction, $\Delta\Gamma_{\rm eff} = \Gamma_{\rm LAT} - \Gamma_{\rm XRT} < \Gamma_2 - \Gamma_1 = \Delta\Gamma$, where Γ_2 and Γ_1 are the asymptotic values of the photon index above and below the cooling break, respectively; or (ii) $\nu_{\rm c}$ can be near or within the LAT energy range, in which case $\Gamma_{\rm LAT} < \Gamma_2$ can be inferred (while $\Gamma_{\rm XRT} = \Gamma_1$), so that again $\Delta\Gamma_{\rm eff} < \Delta\Gamma$. Therefore, imposing $\Delta\Gamma = 0.5$ with a broken power-law spectrum may result in inferred Γ_2 and Γ_1 values that differ from their true values and thus complicate direct comparison to the theoretical prediction for the asymptotic value of Γ_2, which for $p \sim 2$–2.5 corresponds to $\Gamma_2 \sim 2$–2.25.

We examined the influence that a broad cooling break could have on our results by implementing the smoothly broken

power-law (SBPL) spectrum described in Granot & Sari (2002), with a fixed sharpness of the break set to $s = 0.85$. We fit this model to the XRT and LAT data for GRB 130427A and obtained consistent pre- and post-break photon indices of $\Gamma_{\rm BPL1} = 1.54 \pm 0.02$ and $\Gamma_{\rm BPL2} = 2.04 \pm 0.02$, respectively, whereas the SBPL model returned $\Gamma_{\rm BPL1} = 1.56 \pm 0.07$ and $\Gamma_{\rm BPL2} = 2.06 \pm 0.07$. We conclude that the large gap in energy between the XRT and LAT data effectively masks the effects of the curvature in the break energy for the SBPL model as long as the spectral break is well within the MeV domain, resulting in asymptotic photon indices in the XRT and LAT energy ranges that are consistent with those obtained using the simpler BPL model. We present the break energies for the six LAT-detected bursts for which a BPL model was preferred over a PL model in Table 2 and show that the break energies are well above the XRT domain or below the LAT domain, with the exception of GRB 130427A, for which we explicitly fit the SBPL model and showed consistency with the simpler BPL model.

6.2. Constraining the Circumstellar Environment of LAT-detected GRBs

The value and time evolution of the cooling frequency, i.e., the gyration frequency of an electron whose cooling time equals the dynamical time of the system, in an electron synchrotron spectrum in the slow-cooling regime are heavily dependent on the density profile $\rho_{\rm ext}(r) = A_* r^{-k}$ of the circumstellar medium (Chevalier & Li 2000; Granot & Sari 2002). The cooling frequency is expected to evolve to lower energies with time in a constant-density interstellar medium (ISM) ($k = 0$) profile and evolve to higher energies in a stellar wind ($k = 2$) environment.

We speculate that the primary difference between the LAT-detected and nondetected populations may be in the type of circumstellar environment in which these bursts occur. LAT detections may be preferentially selecting GRBs that occur in low wind-like circumburst density profiles for which the synchrotron cooling break begins near the X-ray regime and does not evolve to lower energies; hence, the afterglow spectrum above the X-ray regime remains spectrally hard for longer periods of time.

The inference that LAT-detected bursts may be preferentially occurring in wind-like environments is consistent with an analysis of the multiwavelength observations of both GRB 110731A (Ackermann et al. 2013a) and GRB 130427A (Kouveliotou et al. 2013). Using data collected by the XRT, LAT, and the *Nuclear Spectroscopic Telescope Array* (*NuS-TAR*), Kouveliotou et al. (2013) found that a break between the X-ray and gamma-ray regimes best fits the broadband data for GRB 130427A at very late times. The authors speculate that the cooling break in the afterglow spectra of GRB 130427A may not have evolved with time and remained between the XRT and LAT energy ranges owing to a circumstellar density profile that is intermediate between ISM and wind-like circumstellar density profiles.

Likewise, Ackermann et al. (2013a) performed broadband modeling of optical, UVOT, BAT, XRT, and LAT data associated with GRB 110731A and found that initially a single power law adequately fit the broadband SED using BAT, GBM, and LAT data. At a later time a spectral break was observed between the XRT and LAT data, which was interpreted as a cooling break evolving from low to high

frequencies for a GRB blast wave evolving in a wind-like environment. Although they concluded that an observed break between the optical and X-ray data can be best explained by the presence of a cooling break between the two regimes, the photon index of $\Gamma = 1.77$ obtained through our joint spectral fits for this burst suggests that this break lies above the LAT energy range. Again, the differences between the Ackermann et al. (2013a) work and this analysis can be likely attributed to the greater sensitivity at low energies of the Pass 8 data used in this work, although we point out that our analysis does not include fits to optical data as were performed by Ackermann et al. (2013a).

A preference for LAT-detected GRBs to occur in low-density wind-like circumstellar environments was also found by Cenko et al. (2011), who modeled the broadband spectral and temporal X-ray, optical, and radio afterglow data of four LAT-detected GRBs: GRB 090323, GRB 090328, GRB 090902B, and GRB 090926A. The authors found that a wind environment best fit the data for all but GRB 090902B, for which a constant-density ISM environment was preferred. In this interpretation, the relatively small number of *Swift* XRT-detected bursts that have the expected afterglow behavior in a wind-like density profile (Schulze et al. 2011) may further explain the relatively small number of LAT detections of bright XRT-detected afterglows.

6.3. Constraints on Inverse Compton Emission

The results summarized in Figure 2 significantly constrain the strength and ubiquity of inverse Compton (IC) emission in the 0.1–100 GeV energy range during the XRT and LAT observations that we considered. Such emission is a natural consequence of nonthermal relativistic blast waves thought to power GRB afterglows, although a definitive detection of IC emission at GeV energies has been elusive in the *Fermi* era. IC components can result from upscattering of soft X-ray photons external to the relativistic blast wave, external inverse Compton (EIC; Fan & Piran 2006; He et al. 2012; Beloborodov et al. 2014), or synchrotron self-Compton (SSC), in which synchrotron-emitting electrons in the relativistic blast wave upscatter their own synchrotron radiation (Dermer et al. 2000; Sari & Esin 2001; Zhang & Mészáros 2001; Wang et al. 2013). The lack of significant emission in the LAT energy range in excess of the flux expected from the spectra extrapolated from XRT observations requires that any accompanying IC components must be subdominant to the high-energy tail of the synchrotron spectrum, or peak above the LAT energy range we considered for this analysis.

We can examine these constraints more closely if we consider that the ratio of the peak flux of the synchrotron and SSC components, or Compton Y parameter, in the slow-cooling regime scales as $\propto (\epsilon_e/\epsilon_B)^{1/2}(\gamma_m/\gamma_c)^{p-2}$. Here ϵ_e and ϵ_B are the fractional-energy densities of the relativistic electrons and magnetic field, and γ_m and γ_c represent the minimum injection energy and the typical electron Lorentz factor above which the relativistic electrons radiate a significant fraction of their energy on the dynamical timescale, respectively (Sari & Esin 2001). A relativistic blast wave with a large fraction of its total energy stored in energetic electrons (large ϵ_e) and/or low magnetic field density (extremely small ϵ_B), is expected to generate prominent SSC emission, which is in disagreement with our observations. This could point to a blast wave in the synchrotron-dominated regime in which a larger fraction of

its total energy is stored in the magnetic field density (large ϵ_B; Zhang & Mészáros 2001). Alternatively, the blast wave could be in the Klein–Nishina-dominated regime in which $Y < 1$, even though $\epsilon_e/\epsilon_B \gg 1$ because of the Klein–Nishina reduction to the electron–photon scattering cross section. Both scenarios could suppress the SSC component, making it undetectable in the LAT energy range.

On the other hand, the peak frequency of the SSC component scales roughly as $E_{pk}^{\rm SSC} = \gamma_c^2 E_{pk}^{\rm syn}$, with $E_{pk}^{\rm syn} = E_c$ in the slow-cooling regime, where E_c is the energy of the cooling break. Therefore, a nondetection of strong SSC emission could also imply that $E_{pk}^{\rm SSC}$ is beyond the LAT energy range we considered. Assuming that $E_{pk}^{\rm syn}$ lies between or above the XRT and LAT energy range during our observations, this could be accommodated with a moderate value of γ_c of 100–1000. We note, however, that since the SSC component is expected to span several orders of magnitude in energy around $E_{pk}^{\rm SSC}$ (Sari & Esin 2001), requiring the spectral upturn due to the SSC component to be above the LAT energy range is far more demanding. Likewise, the nondetection of the SSC component at late times, when the cooling break has potentially evolved into the X-ray regime, places even further constraints on this scenario.

The widely discussed detection of high-energy photons with energies >10 GeV hours after the onset of GRB 130427A has been attributed to SSC emission by Tam et al. (2013) and Wang et al. (2013). Ackermann et al. (2014) and Kouveliotou et al. (2013), on the other hand, both argue that the high-energy light curve and spectra are consistent with a single electron synchrotron spectrum throughout the evolution of the extended emission. Here we draw similar conclusions from the three intervals for which we compared the XRT and LAT data for GRB 130427A. The extension of the XRT spectra overpredicts the emission expected in the 0.1–100 GeV energy range and suggests that a break exists between the two energy ranges. Our joint spectral fit to the first of these three intervals ($t_0 \sim 300$ s post trigger) shows that the broadband SED can be well described by a single electron synchrotron spectrum with a cooling break between the X-ray and gamma-ray regimes, matching the conclusions of Kouveliotou et al. (2013) at much later times.

The nondetection of IC emission is also notable in GRB 100728A and GRB 110213A, both of which were detected by the LAT and showed energetic X-ray flares and a significant X-ray plateau lasting roughly ∼2000 s, respectively. These light curve features have been proposed to be the result of late-time energy injection due to continued activity of the central engine (Burrows et al. 2005b; Fan & Wei 2005; Zhang et al. 2006; Panaitescu 2008), and SSC emission at GeV energies could be expected in such a scenario. For both bursts, our analysis finds that the contemporaneous XRT and LAT observations are consistent with a single spectral component. In the case of GRB 100728A we find weak evidence of a break in the broadband spectrum, consistent with a cooling break in an electron synchrotron spectrum. These results point to synchrotron-dominated emission during the flare and plateau afterglow components, and the nondetection of IC emission again suggests a shocked external medium with a strong magnetic field, an extremely high γ_c value so as to have avoided the production of a dominant SSC component at GeV energies, or a blast wave in the Klein–Nishina-dominated regime so as to suppress electron–photon scattering.

14

7. Conclusions

We have used joint observations by the *Swift* XRT and the *Fermi* LAT of GRB afterglows to investigate the nature of long-lived, high-energy emission observed by *Fermi* LAT. By extrapolating the XRT-derived spectra of *Swift*-detected GRBs, we compared the expected flux in the 0.1–100 GeV energy range to the LAT upper limits for the periods in which the burst position was within the LAT FOV. We found that only a small subset of bursts exhibit afterglow emission that could exceed the LAT detection threshold when extrapolated to the 0.1–100 GeV energy range. Bursts that do result in late-time LAT detections are almost exclusively drawn from afterglows that exhibit emission brighter than $F_{\mathrm{XRT}} \gtrsim 10^{-10}$ erg cm^{-2} s^{-1} and harder than $\Gamma_{\mathrm{XRT}} \lesssim 2$.

Joint broadband spectral fits of XRT and LAT data reveal that a majority of LAT nondetections of relatively bright X-ray afterglows can be explained by an afterglow spectrum with a slightly softer photon index when constrained by both the XRT and LAT data, compared to the photon index derived by fits to the XRT data alone. The remaining LAT nondetections are consistent with a cooling break in the predicted electron synchrotron spectrum between the XRT and LAT energy ranges. Such a break is sufficient to suppress the high-energy emission below the LAT detection threshold. On the other hand, the broadband spectra of LAT-detected bursts are best modeled by spectral components that indicate that the cooling break in the synchrotron spectrum lies either between or above the XRT and LAT energy ranges.

Since the value and time evolution of the cooling frequency in an electron synchrotron spectrum are strongly dependent on the density profile of the circumstellar medium, we speculate that the primary difference between bursts with afterglow detections by the LAT and the nondetected population may be the type of circumstellar environment. Late-time LAT detections may be preferentially selecting GRBs that occur in low-density wind-like circumburst environments for which the synchrotron cooling break begins near the X-ray regime and does not evolve to lower energies, resulting in an afterglow spectrum above the X-ray regime that remains spectrally hard for longer periods of time, enhancing the detectability of the afterglow in the LAT energy range.

We find no evidence of high-energy emission significantly in excess of the flux expected from the spectrum predicted by the electron synchrotron model. In addition, joint spectral fits of contemporaneous XRT and LAT observations of an episode of energetic X-ray flaring in GRB 100728A and a significant X-ray plateau in GRB 110213A find that the XRT and LAT data are consistent with a single spectral component. The lack of excess emission at high energies points to two possibilities: (1) a shocked external medium in which the energy density in the magnetic field is elevated or comparable to that of the relativistic electrons behind the shock, precluding the production of a dominant SSC component in the LAT energy range at late times, or (2) the peak of the SSC emission is beyond the 0.1–100 GeV energy range we considered.

ORCID iDs

M. Ajello https://orcid.org/0000-0002-6584-1703
L. Baldini https://orcid.org/0000-0002-9785-7726
D. Bastieri https://orcid.org/0000-0002-6954-8862
R. Bellazzini https://orcid.org/0000-0002-2469-7063
E. Bissaldi https://orcid.org/0000-0001-9935-8106
J. Cohen-Tanugi https://orcid.org/0000-0001-9022-4232
F. D'Ammando https://orcid.org/0000-0001-7618-7527
A. Domínguez https://orcid.org/0000-0002-3433-4610
A. Franckowiak https://orcid.org/0000-0002-5605-2219
Y. Fukazawa https://orcid.org/0000-0002-0921-8837
S. Funk https://orcid.org/0000-0002-2012-0080
P. Fusco https://orcid.org/0000-0002-9383-2425
F. Gargano https://orcid.org/0000-0002-5055-6395
D. Gasparrini https://orcid.org/0000-0002-5064-9495
N. Giglietto https://orcid.org/0000-0002-9021-2888
M. Giroletti https://orcid.org/0000-0002-8657-8852
S. Guiriec https://orcid.org/0000-0001-5780-8770
M. Kuss https://orcid.org/0000-0003-1212-9998
S. Larsson https://orcid.org/0000-0003-0716-107X
F. Longo https://orcid.org/0000-0003-2501-2270
F. Loparco https://orcid.org/0000-0002-1173-5673
P. Lubrano https://orcid.org/0000-0003-0221-4806
J. D. Magill https://orcid.org/0000-0001-9231-2965
S. Maldera https://orcid.org/0000-0002-0698-4421
A. Manfreda https://orcid.org/0000-0002-0998-4953
M. N. Mazziotta https://orcid.org/0000-0001-9325-4672
T. Mizuno https://orcid.org/0000-0001-7263-0296
M. E. Monzani https://orcid.org/0000-0002-8254-5308
A. Morselli https://orcid.org/0000-0002-7704-9553
N. Omodei https://orcid.org/0000-0002-5448-7577
J. S. Perkins https://orcid.org/0000-0001-9608-4023
M. Pesce-Rollins https://orcid.org/0000-0003-1790-8018
J. L. Racusin https://orcid.org/0000-0002-4744-9898
S. Rainò https://orcid.org/0000-0002-9181-0345
R. Rando https://orcid.org/0000-0001-6992-818X
M. Razzano https://orcid.org/0000-0003-4825-1629
S. Razzaque https://orcid.org/0000-0002-0130-2460
O. Reimer https://orcid.org/0000-0001-6953-1385
C. Sgrò https://orcid.org/0000-0001-5676-6214
G. Spandre https://orcid.org/0000-0003-0802-3453
D. F. Torres https://orcid.org/0000-0002-1522-9065
G. Tosti https://orcid.org/0000-0002-0839-4126

References

Abdo, A. A., Ackermann, M., Ajello, M., et al. 2011, ApJL, 734, L27
Abdo, A. A., Ackermann, M., Arimoto, M., et al. 2009a, Sci, 323, 1688
Abdo, A. A., Ackermann, M., Asano, K., et al. 2009b, ApJ, 707, 580
Acero, F., Ackermann, M., Ajello, M., et al. 2015, ApJS, 218, 23
Ackermann, M., Ajello, M., Albert, A., et al. 2012a, ApJS, 203, 4
Ackermann, M., Ajello, M., Anderson, B., et al. 2016, ApJ, 822, 68
Ackermann, M., Ajello, M., Asano, K., et al. 2013a, ApJ, 763, 71
Ackermann, M., Ajello, M., Asano, K., et al. 2013b, ApJS, 209, 11
Ackermann, M., Ajello, M., Asano, K., et al. 2014, Sci, 343, 42
Ackermann, M., Ajello, M., Baldini, L., et al. 2010, ApJL, 717, L127
Ackermann, M., Ajello, M., Baldini, L., et al. 2012b, ApJ, 754, 121
Arnaud, K. A. 1996, in ASP Conf. Ser. 101, Astronomical Data Analysis
    Software and Systems V, ed. G. H. Jacoby & J. Barnes (San Francisco, CA:
    ASP), 17
Atwood, W. B., Abdo, A. A., Ackermann, M., et al. 2009, ApJ, 697, 1071
Barthelmy, S. D., Barbier, L. M., Cummings, J. R., et al. 2005, SSRv, 120, 143
Beloborodov, A. M., Hascoët, R., & Vurm, I. 2014, ApJ, 788, 36
Beniamini, P., Guetta, D., Nakar, E., & Piran, T. 2011, MNRAS, 416, 3089
Burrows, D. N., Hill, J. E., Nousek, J. A., et al. 2005a, SSRv, 120, 165
Burrows, D. N., Romano, P., Falcone, A., et al. 2005b, Sci, 309, 1833
Cenko, S. B., Frail, D. A., Harrison, F. A., et al. 2011, ApJ, 732, 29
Chevalier, R. A., & Li, Z.-Y. 2000, ApJ, 536, 195
De Pasquale, M., Schady, P., Kuin, N. P. M., et al. 2010, ApJL, 709, L146
Dermer, C. D., Chiang, J., & Mitman, K. E. 2000, ApJ, 537, 785
Evans, P. A., Beardmore, A. P., Page, K. L., et al. 2007, A&A, 469, 379
Evans, P. A., Beardmore, A. P., Page, K. L., et al. 2009, MNRAS, 397, 1177
Fan, Y., & Piran, T. 2006, MNRAS, 370, L24

Fan, Y. Z., & Wei, D. M. 2005, MNRAS, 364, L42
Ghisellini, G., Ghirlanda, G., Nava, L., & Celotti, A. 2010, MNRAS, 403, 926
Granot, J., & Sari, R. 2002, ApJ, 568, 820
He, H.-N., Zhang, B.-B., Wang, X.-Y., Li, Z., & Mészáros, P. 2012, ApJ,
    753, 178
Kouveliotou, C., Granot, J., Racusin, J. L., et al. 2013, ApJL, 779, L1
Kumar, P., & Barniol Duran, R. 2009, MNRAS, 400, L75
Mattox, J. R., Bertsch, D. L., Chiang, J., et al. 1996, ApJ, 461, 396
Maxham, A., Zhang, B.-B., & Zhang, B. 2011, MNRAS, 415, 77
Neyman, J., & Pearson, E. S. 1928, Biometrika, 20, 175
Panaitescu, A. 2008, MNRAS, 383, 1143
Racusin, J. L., Liang, E. W., Burrows, D. N., et al. 2009, ApJ, 698, 43
Racusin, J. L., Oates, S. R., de Pasquale, M., & Kocevski, D. 2016, ApJ,
    826, 45
Racusin, J. L., Oates, S. R., Schady, P., et al. 2011, ApJ, 738, 138
Razzaque, S., Dermer, C. D., & Finke, J. D. 2010, OAJ, 3, 150
Roming, P. W. A., Kennedy, T. E., Mason, K. O., et al. 2005, SSRv, 120, 95
Sari, R., & Esin, A. A. 2001, ApJ, 548, 787
Schulze, S., Klose, S., Björnsson, G., et al. 2011, A&A, 526, A23
Tam, P.-H. T., Tang, Q.-W., Hou, S.-J., Liu, R.-Y., & Wang, X.-Y. 2013,
    ApJL, 771, L13
Vianello, G., Omodei, N. & Fermi/LAT Collaboration 2015, arXiv:1502.
    03122
Wang, X.-Y., Liu, R.-Y., & Lemoine, M. 2013, ApJL, 771, L33
Wilks, S. S. 1938, Ann. Math. Stat., 9, 60
Yassine, M., Piron, F., Mochkovitch, R., & Daigne, F. 2017, A&A, 606, A93
Zhang, B., Fan, Y. Z., Dyks, J., et al. 2006, ApJ, 642, 354
Zhang, B., & Mészáros, P. 2001, ApJ, 559, 110
Zhang, B.-B., Zhang, B., Liang, E.-W., et al. 2011, ApJ, 730, 141